Supplementary Material (ESI) for CrystEngComm

Supporting Information for

Macrostructural Microporous Calcium Carbonate Tetragonal Prisms: Top-Down Solid-Phase Fabrication and Application as Phase-Change Support Matrices

Shudong Zhang, Min Zhou, Xia Lu, Changzheng Wu, Yongfu Sun, Yi Xie *

Department of Nanomaterials and Nanochemistry, Hefei National Laboratory for Physical Sciences at Microscale, University of Science and Technology of China, Hefei, Anhui 230026, P. R. China.

** To whom correspondence should be addressed. Tel& Fax: 86-551-3603987.*

E-mail: yxie@ustc.edu.cn

S1. A corresponding digital camera images showing the effects of heat on the pyrogenation process of L-ascorbic acid and growth of high-quality COD microcrystals

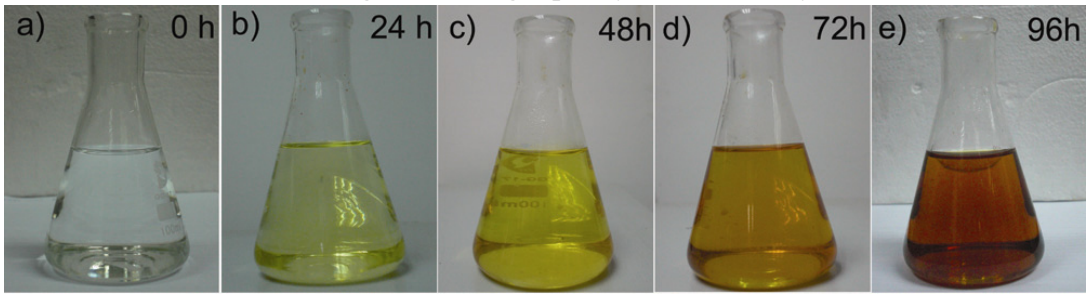

Figure S1. Pictures showing that the solution color change processes from colorless to brick red are a step-by-step process.

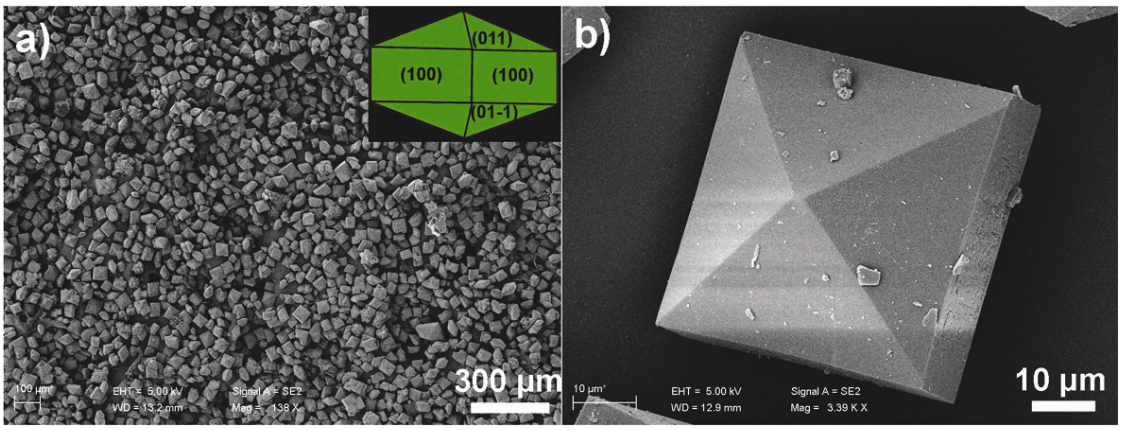

Figure S2. Low magnification FESEM image (a) and a detail view of an individual high-quality COD microcrystal (b) obtained at pH = 5. Inset: schematic illustration of the morphology of COD microcrystals.

S2. The influences of the pH values and the temperature on the shapes of COD microcrystals.

we have demonstrated L-ascorbic acid (AA), which has potentials to serve as the $C_2O_4^{2-}$ source, was used to obtain high-quality calcium oxalate dehydrate (COD) tetragonal prisms for the first time. It has been shown that with increasing pH value of solution, the morphology of the obtained COD crystals gradually changed from tetragonal prisms dominated by the {101} faces to rodlike tetragonal prisms dominated by the {100} faces. The composition and phase purity of the products were first examined by XRD. Figure S3 shows representative XRD patterns of the as-prepared COD samples at 80 °C for 4 days under various pH conditions of pH = 7 and pH = 9. The diffraction peaks of the two samples can be indexed as a pure tetragonal COD phase (space group I4/ m), which coincides well with the literature values (JCPDS No. 87-0655). It is worth pointing out that the XRD patterns also indicate that there is a large difference from each other in the relative intensities based on (200), (202), and (141) peaks for two samples, indicating the possibility of different preferential orientation growth under different pH conditions.

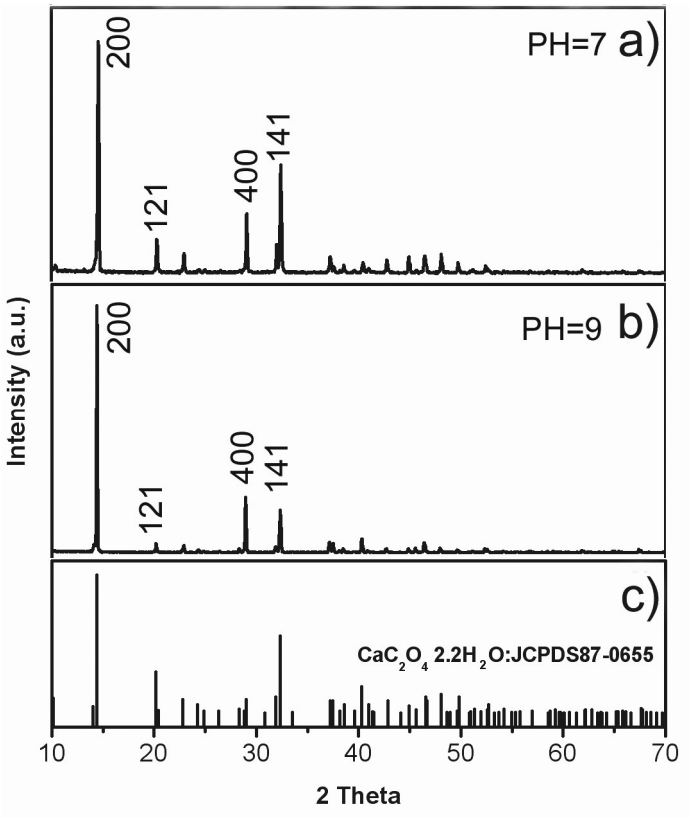

Figure S3. The XRD patterns of the as-prepared COD products at different pH values at 80 °C for 4 days at the different pH value of (a) pH = 7, (b) pH = 9, and (c) the standard data of tetragonal COD (JCPDS 87-0655).

The morphology of the products was studied by the field emission scanning electron microscopy as shown in Figure S4. The SEM images provide direct information about the size and typical shapes of the as-synthesized COD samples under different conditions. Figure S4 illustrates the representative SEM images of COD prepared at different pH values. The product obtained at pH = 5 is composed of a general deal of tetragonal COD prisms with a uniform size (Figure 2 in text). With the pH values increased, the tetragonal prisms were further elongated along the c-axis, resulting in elongated tetragonal COD microcrystals (Figure S4a). It can be observed that the elongated tetragonal COD microcrystals were rather uniform with an average side length and width of 25 μm * 40 μm, which showed an aspect ratio as high as about 2. The corresponding XRD pattern (Figure S3a) shows largely intensified (200) and (400) peaks of COD, suggesting a preferential alignment of the (100) plane, which is consistent with the SEM observation that the tetragonal COD prisms generally lay on the {100} planes. As the pH value was increased to 9, the tetragonal prisms were further elongated along the c-axis, engendering rodlike tetragonal prisms (Figure S4c). It can be observed that the elongated tetragonal prisms were rather uniform with the average side length of 3 μm and their average side width of 15 μm, which indicated an aspect ratio as high as 5. Occasionally, twinning of rodlike tetragonal prisms was also observed. The XRD pattern shown in Figure S3b also reveals the appearance of only (200) and (400) peaks of COD, confirming the formation of the rodlike tetragonal prisms dominated by the {100} faces of COD.

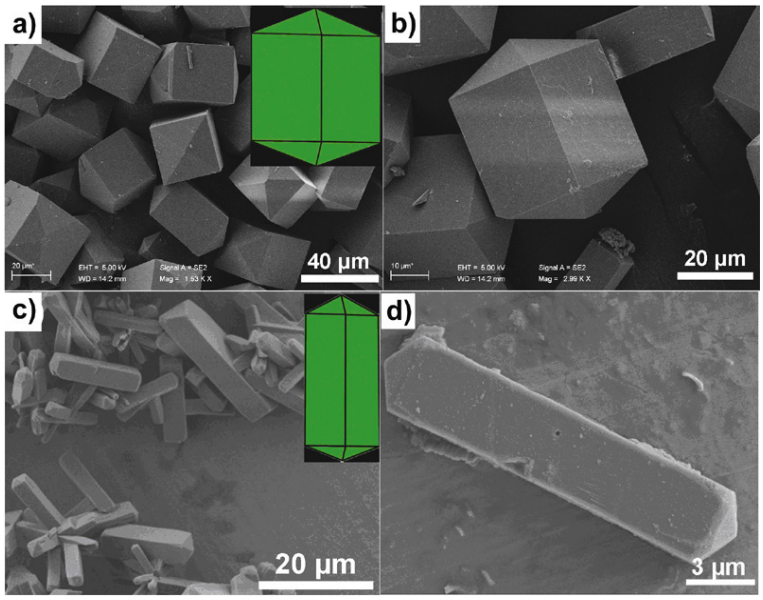

Figure S4. The influence of the pH values on the shapes of COD microcrystals. Low magnification FESEM image (a, c,) and a detail view of an individual high-quality COD microcrystal (b, d). (a, b) Elongated tetragonal COD prisms obtained at pH =7. (c, d) Tetragonal COD microrods obtained at pH = 9. Inset: schematic illustration of the different morphology of COD microcrystals.

In addition, the different morphology of COD microcrystals could also be controlled by the different reaction temperature. As the reaction temperature was decreased to 60 °C at pH = 5, the tetragonal COD prisms were obtained, which is the accordant with the samples obtained at the temperature of 80 °C (Figure 4 in text). When the reaction temperature was increased at 100 °C at ph = 5, 1 D rodbundle-like structures were obtained, as shown in Figure S5a, b. Figure S5a shows the low-magnification SEM image of typical composition of a very uniform, rodbundle-like architecture. The detailed morphology of the rodbundle-like micro-nanostructure is shown in Figure S3b, which are composed of a large quantity of the nanowires with square-shape have uniform size and smooth surface. And as shown in Figure S5c-d, 1 D rodlike COD structures were obtained at the reaction temperature of 120 °C. Figure S5c shows the low-magnification SEM image of typical composition of very uniform1D nanowires architecture of 20 μm in length. The detailed morphology of 1D nanowires is shown in Figure S3d, which are composed of a large quantity of one-dimensional nanoplates with a width of about 700 nm and an average length of about 15 μm. The all results confirmed that temperature is a critical factor for the formation of the morphology of COD microstructures. Therefore, the reaction temperature also plays a pivotal role in the synthesis process and control of the morphology of the COD nanostructures. More in-depth studies are necessary to further understand their growth process.

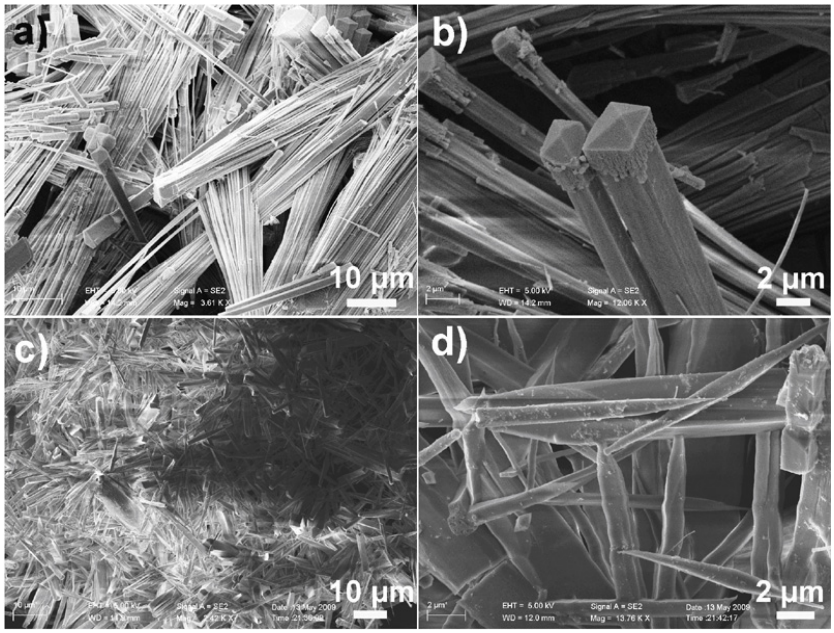

Figure S5. At pH= 5, (a) and (c) Low- and (b) and (d) high-magnification FESEM images of the as-prepared COD samples obtained in the temperature of 100 and 120 °C, respectively.

It is evident that the COD nucleation and growth process in our reaction system is consistent with the previous reports on the mineralization of witherite crystals [S1]. The nucleation process in our current system mainly depends on supersaturation (σ) of the solution [S2], which can be defined by eq 1

$$\sigma \equiv \Delta\mu/k_BT = \ln(\alpha/\alpha_c) \qquad (1)$$

or for CaC_2O_4 in aqueous solution, the superaturation can be defined by eq 2

$$\sigma = \ln(a(Ca^{2+})\alpha(C_2O_4^{2-})/K_{sp}) \quad (2)$$

where Δμ stands for the change in chemical potential per molecule, k_B is the Boltzmann constant, T is absolute temperature, α and α_c are actual and equilibrium activity products, $\alpha(Ca^{2+})$ is the activity of Ca^{2+}, $\alpha(C_2O_4^{2-})$ is the activity of $C_2O_4^{2-}$, and K_{sp} is the equilibrium solubility product at zero ionic strength of the experimental solutions at current experimental temperature.

In growth process of COD microcrystals, the nucleation mainly depends on the supersaturation of the solution and is determined by activity of Ca^{2+} and $C_2O_4^{2-}$. Different from non-equilibrium nucleation condition that takes place when $C_2O_4^{2-}$ added into the solution directly, the nucleation process under thermolysis possesses a more stable nucleation rate. Because the thermolysis velocity is relatively slow and depends on the temperature that remains constant during the growth process, the nucleation rate is stable and relatively slow during the current growth process. Meanwhile, in growth process of COD microcrystals, L-ascorbic acid performed double roles as a $C_2O_4^{2-}$ source, and a structure directing templates as other organic acid [S3]. L-ascorbic acid maybe stabilize the (100) plane depending on its net-charge, which depends on pH and temperature. Under the different circumstance of thermolysis, the different nucleation behavior in addition to the adsorption of ions or molecules during the growth process would lead to the generation of

different kinds of COD crystals. And more in depth studies are necessary in order to understand the different growth patterns at the different conditions.

S3. SrC_2O_4 and BaC_2O_4 with hierarchical order were synthesized in the same reaction system.

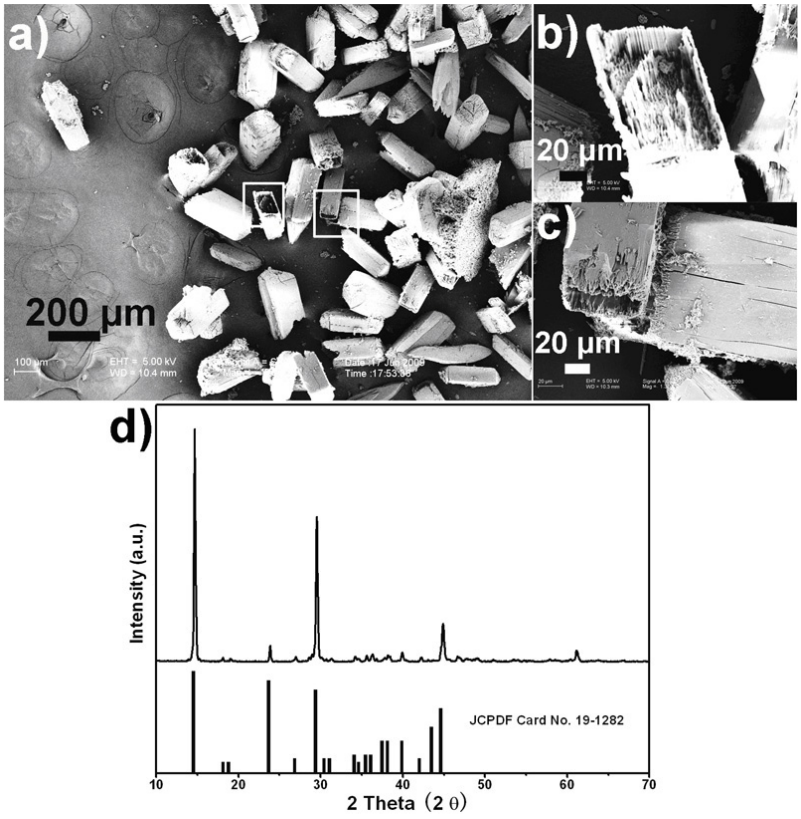

Figure S6. Characterizations of the as-prepared SrC_2O_4·? H_2O products. Low-magnification SEM image (a), High-magnification FESEM images (b) and (c). XRD pattern (d) and the standard data of monoclinic SrC_2O_4·? H_2O (JCPDS 19-1282).

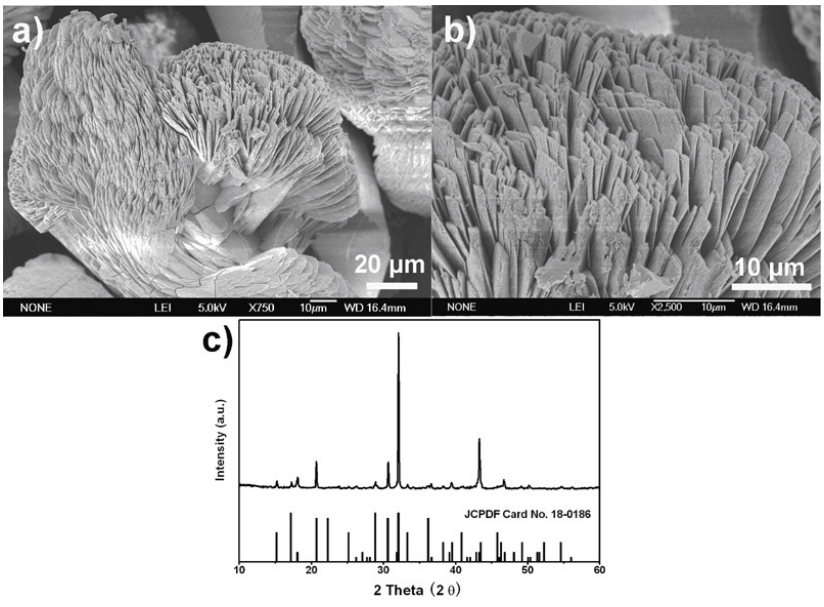

Figure S7. Characterizations of the as-prepared BaC_2O_4·? H_2O products. Low-magnification SEM image (a), High-magnification FESEM image (b). XRD pattern and the standard data of BaC_2O_4·? H_2O (JCPDS 18-0186) (c).

S4. The crystal structure of COD.

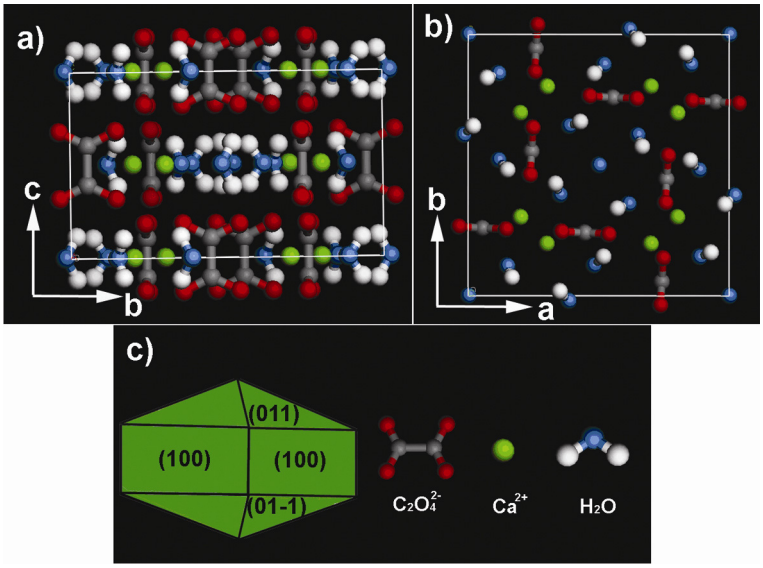

Figure S8. COD crystallographic projections of the (100) (a) and (001) (b) planes calculated from the crystal structure , (c) schematic illustration of the (100) and (01-1) faces of tetragonal prism.

S5. The variable temperature X-ray diffraction and DSC curve of the COD microcrystals.

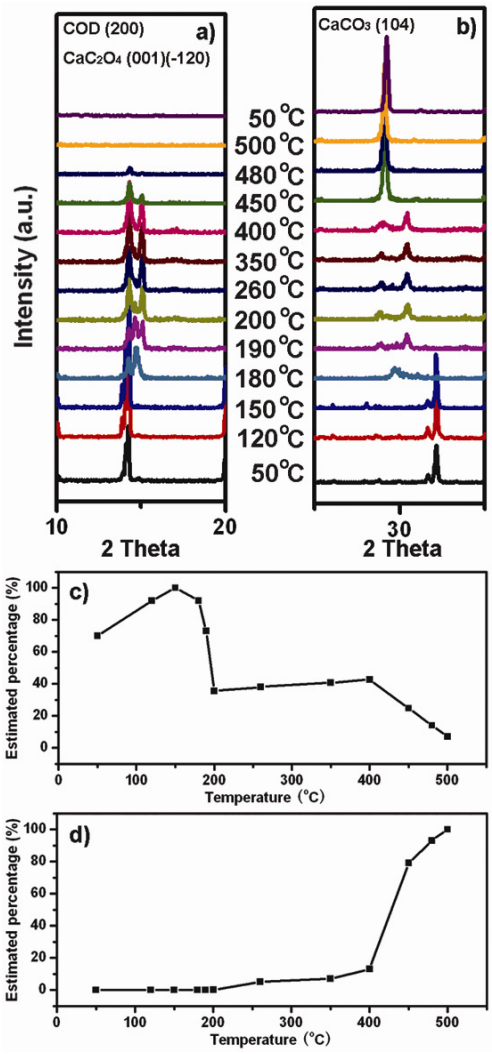

Figure S9. The peak (200) of COD (a) and the peak (104) of $CaCO_3$ (b) XRD analysis for temperature-dependent decomposition of COD from 50 to 500 °C. The peak (200) of COD (c) and (104) of $CaCO_3$ (d) intensities as a function of reaction temperature indicate the decomposition from COD to $CaCO_3$.

The temperature-dependent decomposition of COD in Figure S8a shows that the (200) peak of COD decreases slowly, splits into two (001) and (-120) peaks of α-CaC_2O_4, and eventually disappears with temperature increasing from 50 °C to 500 °C. On the contrary, as shown in Figure 6b, the (104) peak of as-decomposed $CaCO_3$ product appears slowly and eventually increases with the increased temperature. The results are also presented in Figure S8c and S8d by monitoring the (200) and (104) peak intensity as a function of temperature, respectively. The (200) peak intensity appears to have a decline trend after an initial ascent due to the increased crystallinity and eventually disappears with the increase of temperature from 50, 120, 150, 180, 190, 200, 260, 350, 400, 450, 480 to 500 °C (Figure S8c). In other words, the higher quality COD microcrystals are obtained before the thermal decomposition process of COD microcrystals took place. At the same time, as shown in Figure S8d, the (104) peak intensity of as-obtained $CaCO_3$ appears slowly and eventually increases with the increase of temperature from 50, 120, 150, 180, 190, 200, 260, 350, 400, 450, 480 to 500 °C.

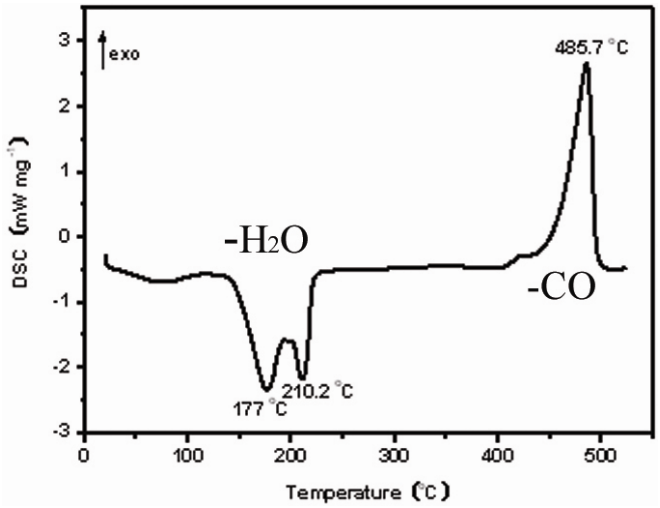

Figure S10. DSC plot of the COD microcrystals under nitrogen at the heating rate of 10 $Kmin^{-1}$.

The so-obtained DSC curve of the COD microcrystals is reported in Figure S6. As displayed in Figure S6 for COD products, endothermic and exothermic peaks of DSC curves were observed at around 120 ~ 250 °C and 400 ~ 520 °C, respectively, which coincides quite well with the value extracted from the TGA measurements.

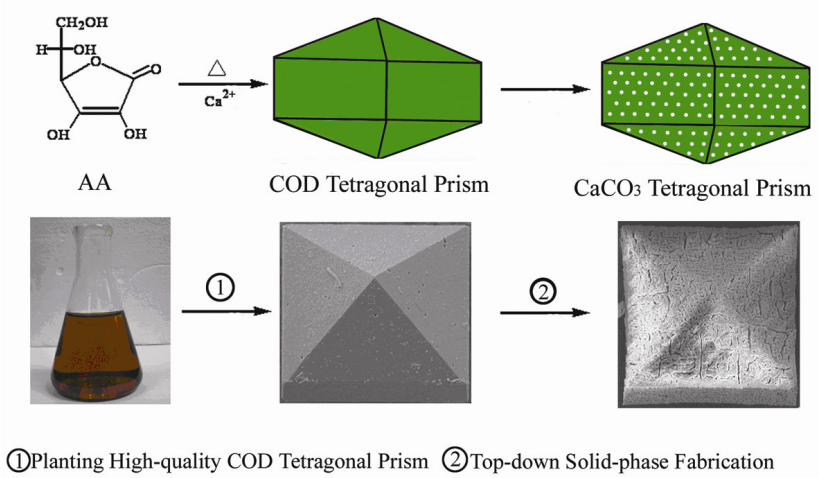

Scheme S1. A schematic illustration exhibits the formation of microporous $CaCO_3$ tetragonal prisms. It involves the initial planting of high-quality COD tetragonal prisms □, and eventual top-down solid-phase fabrication of microporous $CaCO_3$ tetragonal prisms □ at the different heating rate.

S6. The BET isotherms and their corresponding pore size distribution curves of as-decomposed $CaCO_3$ microporous tetragonal prisms.

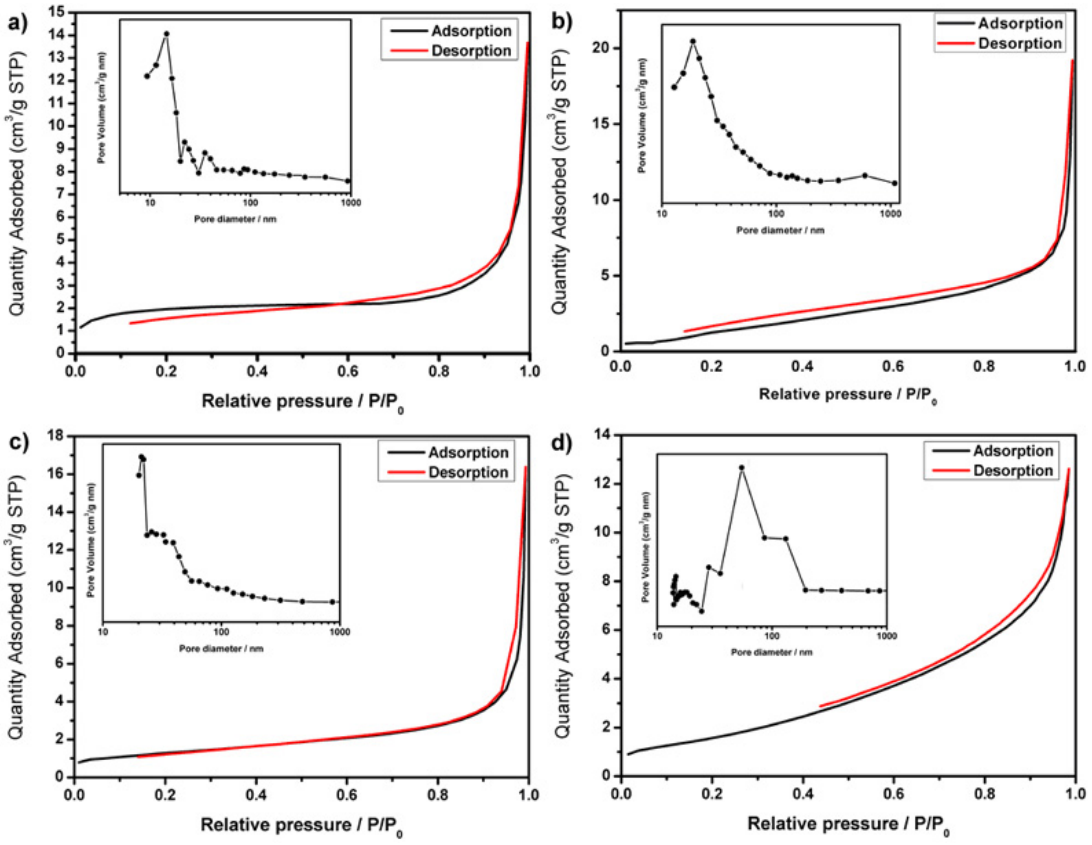

Figure S11 Adsorption/desorption isotherms of nitrogen and their corresponding pore size distribution curves of as-decomposed $CaCO_3$ microporous tetragonal prisms at the different heating rate of (a) 2 °C min^{-1}, (c) 10 °C min^{-1}, (e) 20 °C min^{-1}, and 500 °C min^{-1}, repectively (see Figure 4 in the text).

Table S1. Average pore diameter and BET surface area of the different $CaCO_3$ samples.

Sample No.	1	2	3	4
Heating rate (°C/min)	2	10	20	500
BET surface area (m^2g^{-1})	13.6	5.8	4.6	4.2

Table S1 shows the BET-surface area of the different mesoporous $CaCO_3$ obtained at different calcined rate. $CaCO_3$ samples calcined at 2 °C/min reach the maximal surface area of 13.6 m^2 g^{-1}. Whereas, when calcined at a higher rate, lower BET surface area of $CaCO_3$ samples was obtained. And theoretical calculation of the surface area of nonporous $CaCO_3$ tetragonal prisms with the same average size gives us the value of 0.07 m^2 g^{-1}. Thus, for $CaCO_3$ tetragonal prisms used in our work we have a surface area that is 194, 82, 65, and 60 times larger due to porous structure, respectively, which is significantly higher than that of $CaCO_3$ microspheres reported [S4], implying the existence of mesoporous structure.

References:

S1. Y. Zhao, Y. Xie,,S. Yan, and Y. W. Dong, *Crystal Growth & Design,***2009**, *9,* 3072-3078

S2. (a) J. I. Drever, *The Geochemistry of Natural Waters: Surface and Groundwater Environments*; Prentice Hall: Upper Saddle River, NJ, 1997. (b) K. J. Davis, P. M. Dove, J. J. De Yoreo, Science **2000**, *290*, 1134–1137.

S3. H. Tong, W. T. Ma, L. L. Wang, P. Wan, J. M. Hu, L. X. Cao, *Biomaterials,* **2004**, *25*, 3923.

S4. (a) G. B. Sukhorukov, D. V. Volodkin, A. M. Günther, A. I. Petrov, D. B. Shenoy, H. Möhwald, *J. Mater. Chem.,* **2004,** *14,* 2073.; (b) D. V. Volodkin, A. I. Petrov, M. Prevot, G. B. Sukhorukov, *Langmuir,* **2004,** *20,* 3398.